ACS Catalysis

Research Article

pubs.acs.org/acscatalysis

# Enhanced Visible-Light Photocatalytic Activity of BiOI/BiOCl Heterojunctions: Key Role of Crystal Facet Combination

Liming Sun,[⊥,†,‡] Li Xiang,[⊥,†] Xian Zhao,[§] Chun-Jiang Jia,[†] Jun Yang,[∥] Zhao Jin,[†] Xiufeng Cheng,[§] and Weiliu Fan*[,†]

[†]Key Laboratory for Colloid and Interface Chemistry of State Educating Ministry, School of Chemistry and Chemical Engineering, Shandong University, Jinan 250100, People's Republic of China

[‡]Department of Chemistry, School of Chemistry and Chemical Engineering, Jiangsu Normal University, Xuzhou 221116, People's Republic of China

[§]State Key Laboratory of Crystal Materials, Shandong University, Jinan 250100, People's Republic of China

[∥]State Key Laboratory of Multiphase Complex Systems, Institute of Process Engineering, Chinese Academy of Sciences, Beijing 100190, People's Republic of China

Supporting Information

**ABSTRACT:** Two comparable models of BiOI/BiOCl heterojuctions with different interface structures (crystal surface orientation and crystal surface combination), denoted as $BiOI_{(001)}/BiOCl_{(001)}$ and $BiOI_{(001)}/BiOCl_{(010)}$, have been prepared via integrating heterojuncton nanostructure construction with crystal facet engineering. $BiOI_{(001)}/BiOCl_{(010)}$ had a greater degree of lattice mismatch and displayed higher visible-light photocatalytic activity than $BiOI_{(001)}/BiOCl_{(001)}$. In general, the activity of a photocatalyst ($\eta_{PC}$) has a positive correlation with light harvesting ($\eta_{LH}$), charge separation ($\eta_{CS}$), and charge injection ($\eta_{CI}$). On the basis of the experimental results, we considered that the higher $\eta_{CI}$ value of $BiOI_{(001)}/BiOCl_{(010)}$ was the main reason for its better visible-light photocatalytic performance. In combination with theoretical calculations, we found that the higher $\eta_{CI}$ value of $BiOI_{(001)}/BiOCl_{(010)}$ was the result of a shorter photogenerated electron diffusion distance, assisted by the self-induced internal electric fields of the BiOCl slabs. This indicated that the crystal facet combination is the key to enhancing the photocatalytic activity of BiOI/BiOCl. Our work offers an archetype for the further design of heterojunction photocatalysts with a fine tuning of the interface structures in order to reach optimized charge injection and enhanced photocatalytic activity.

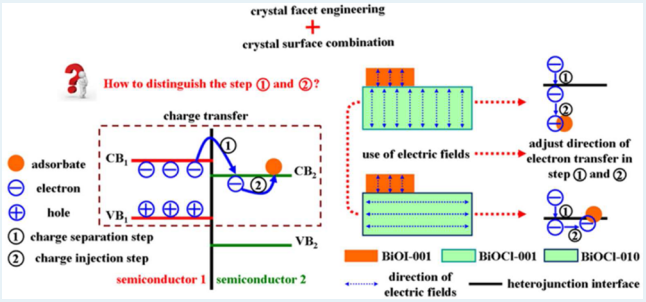


**KEYWORDS:** *heterojunction photocatalysts, crystal facet engineering, internal electric fields, directional transfer of carriers, first-principles study*

## 1. INTRODUCTION

Semiconductor photocatalysts have attracted worldwide attention for their potential in solving energy and environmental issues.[1−9] However, up to now, the efficiency of photocatalysis is still too low for its use in practical apllications. Because a large number of traditional photocatalysts are active only in the ultraviolet region, they suffer from wide band gaps and have only moderate performance originating from a high recombination rate of photogenerated electron−hole pairs.[10−13] Generally, heterojunction photocatalysts composed of narrow-band-gap semiconductors and wide-band-gap semiconductors with interlaced band structures achieve better visible-light response and efficient separation of the electron−hole pairs.[14−22] Thus, recent years have witnessed a flourish of interest in the construction of various heterojunction structures toward enhancing the photocatalytic performance of semiconductors for solar energy conversion.

Previous studies have showed that the lattice and band match are two important factors for fabricating stable and efficient heterojunction photocatalysts.[19] On the basis of these two factors, most recent heterojunction photocatalytic studies have focused on the control of morphology and the net efficiency of increasing the overall photocatalytic activity. In general, the photocatalytic activity of a heterojunction ($\eta_{PC}$) has a positive correlation with light harvesting ($\eta_{LH}$), charge separation ($\eta_{CS}$), and charge injection ($\eta_{CI}$).[23−26] After determination of the composition of the heterojunction, the value of $\eta_{LH}$ is fixed and treated as a constant. Thus, increasing both $\eta_{CS}$ and $\eta_{CI}$ is the key to improved performance in heterojunction photocatalysts. However, due to the complexity and rapidity of the photocatalytic reaction, it is difficult to control charge transfer

Received: October 22, 2014
Revised: April 22, 2015
Published: May 4, 2015




DOI: 10.1021/cs501631n
ACS Catal. 2015, 5, 3540−3551

behavior in both charge separation and charge injection steps. Most enhancement of the photocatalytic activity of heterojunctions has been achieved by improving $\eta_{CS}$ for the charge separation step,[27] whereas methods to increase $\eta_{CI}$ for the charge injection step when followed by a charge separation step to further enhance the photocatalytic performance of heterojunctions are not known. The development of a simple and effective method to improve $\eta_{CI}$ would open up new possibilities for the design of higher efficiency heterojunction photocatalysts.

The use of electric fields to control the direction of charge transfer in the separation and injection steps within photocatalyst materials can be realized by integrating crystal facet engineering with crystal surface combination and is an effective strategy for improving $\eta_{CS}$ and $\eta_{CI}$. In bismuth oxyhalides (BiOX, X = Cl, Br, I), the internal static electric fields between the $[Bi_2O_2]^{2+}$ slabs and the halogen anionic layers enable effective separation of photogenerated electron−hole pairs along the *c* axis,[28−37] and these are suitable materials to verify our proposed idea.

In this study, using the BiOI/BiOCl heterojunction as an example, we designed and synthesized two comparable models with different interface structures, denoted $BiOI_{(001)}/BiOCl_{(001)}$ and $BiOI_{(001)}/BiOCl_{(010)}$, by combining heterojunction nanostructure construction with crystal facet engineering. The schematic illustrations of these two BiOI/BiOCl heterojunctions are shown in Figure 1. $BiOI_{(001)}/BiOCl_{(010)}$ displayed a

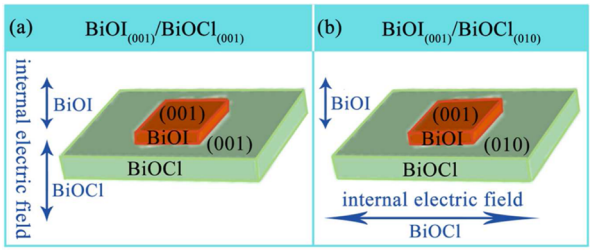


**Figure 1.** Schematic illustrations of $BiOI_{(001)}/BiOCl_{(001)}$ (a) and $BiOI_{(001)}/BiOCl_{(010)}$ (b) heterojunction photocatalysts.

visible-light photocatalytic activity higher than that of $BiOI_{(001)}/BiOCl_{(001)}$, though its degree of lattice mismatch was greater. The photoelectrochemical results suggested that the higher $\eta_{CI}$ value was the main reason for the superior photocatalytic performance of $BiOI_{(001)}/BiOCl_{(010)}$. Using experimental data and theoretical calculations, we present visualized evidence that shows that the shorter photogenerated electron diffusion distance in the self-induced internal electric fields of BiOCl slabs leads to higher $\eta_{CI}$ of $BiOI_{(001)}/BiOCl_{(010)}$. Our work highlights that, beyond achievement of lattice and band match, increasing the efficiency of photogenerated charge transfer by adjusting the interface microstructure can also significantly improve the photocatalytic activity of heterojunctions. Our study should facilitate a deeper understanding of charge transfer behavior in heterojunction photocatalysts and provide a reference for the design of higher efficiency heterojunction photocatalysts.

## 2. EXPERIMENTAL SECTION

**2.1. Preparation of Photocatalysts.** BiOI nanosheets were synthesized by a facile chemical bath method at low temperature. Typically, 4 mmol of KI (Sinopharm Chemical Reagent Co., Ltd., 99.0%) was dissolved in 35 mL of deionized water, and then 4 mmol of $Bi(NO_3)_3{\cdot}5H_2O$ (Sinopharm Chemical Reagent, 99.0%) was added to this solution and the mixture was stirred for 30 min at room temperature. Subsequently, the mixture was heated at 80 °C for 2 h in a water bath. Finally, the resulting precipitate was collected, washed thoroughly with deionized water and ethanol, and dried at 60 °C in air.

BiOCl nanosheets were synthesized using a hydrothermal method.[38] In a typical synthesis of BiOCl nanosheets with exposed (010) surfaces, denoted as BiOCl-010, 4 mmol of $Bi(NO_3)_3{\cdot}5H_2O$ and 4 mmol of KCl (Sinopharm Chemical Reagent Co., Ltd., 99.5%) were added to 30 mL of deionized water, and the mixture was stirred for 30 min at room temperature. Then 2 mol $L^{-1}$ NaOH (Sinopharm Chemical Reagent Co., Ltd., 99.0%) was added to this mixture to adjust the pH value to 6.0. After it was stirred for another 30 min at room temperature, the mixture was poured into a 50 mL autoclave with an inner Teflon lining, maintained at 160 °C for 24 h, and then cooled to room temperature. The resulting precipitate was collected, washed thoroughly with ethanol and deionized water, and dried at 60 °C in air. The BiOCl nanosheets with exposed (001) surfaces, denoted as BiOCl-001, were prepared using the same procedure, without the addition of NaOH.

For the preparation of the $BiOI_{(001)}/BiOCl_{(010)}$ heterojunction, 0.211 g of BiOI and 0.364 g of BiOCl-010 were each dispersed in 10 mL of ethanol for 30 min under ultrasonication. Then, the BiOI and BiOCl-010 suspensions were mixed together and simultaneously agitated using a magnetic stirrer. After volatilization of the solvent, the resultant samples were collected and calcined at 250 °C for 3 h to provide enough thermal energy to achieve a tight chemical binding between the BiOI and BiOCl-010 powders. The $BiOI_{(001)}/BiOCl_{(001)}$ heterojunction was prepared using the same procedure with BiOCl-001 instead of BiOCl-010.

**2.2. Characterization.** Powder X-ray diffraction (XRD) patterns were obtained on a D8 Advance X-ray diffractometer (Bruker Germany), using Cu K$\alpha$ radiation at a scan rate of 0.02° (2$\theta$) $s^{-1}$. Scanning electron microscopy (SEM) was performed with an S-4800 field emission SEM instrument (FESEM, Hitachi, Japan) at an accelerating voltage of 5 kV. High-resolution transmission electron microscopy (HRTEM) analyses were conducted with a JEM 2100 microscope at an accelerating voltage of 200 kV. X-ray photoelectron spectroscopy (XPS) and valence band X-ray photoelectron spectroscopy (VB XPS) were performed on an ESCALAB 250 spectrometer equipped with an Al K$\alpha$ source. Ultraviolet−visible (UV−vis) diffuse reflectance spectroscopy (DRS) was carried out using a UV−vis spectrophotometer (Shimadzu UV-2550, Japan), using $BaSO_4$ as the reference sample. Nitrogen adsorption isotherms were measured with an ASAP 2020 adsorption analyzer (Micromeritics) at liquid nitrogen temperature. Prior to the measurements, the samples were degassed at a temperature of 77 K for 10 h. The Brunauer−Emmett−Teller (BET) surface area was determined from the relative pressure range 0.06−0.2.

**2.3. Photocatalytic Experiments.** The photocatalytic activities of the as-prepared samples were evaluated by the degradation of methyl orange (MO) and phenol under visible-light irradiation at ambient temperature using a 300 W metal halide lamp with a 420 nm cutoff filter as the light source. In each experiment, 50 mg of photocatalyst was dispersed in an


DOI: 10.1021/cs501631n
ACS Catal. 2015, 5, 3540−3551

MO (100 mL, 20 mg $L^{-1}$) or phenol (100 mL, 30 mg $L^{-1}$) aqueous solution. Prior to irradiation, the solution was continuously stirred in the dark for 1 h to ensure the establishment of an adsorption−desorption equilibrium between the photocatalysts and the degrading pollutants. During the photoreactions, the MO or phenol solutions with photocatalysts were continuously stirred with dynamoelectric stirrers, and 5 mL aliquots were taken from each sample every 30 min, followed by centrifugation and filtration to remove the photocatalysts. The concentrations of MO and phenol were determined by monitoring the change of optical density at 465 and 270 nm, respectively, with a Hitachi U-3500 UV−vis spectrometer.

**2.4. Photoelectrochemical Measurements.** The photocurrents were measured with an electrochemical workstation (LAN-LIKE, Tianjin, People's Republic of China) in a standard three-electrode system with the sample as the working electrode, a Pt foil as the counter electrode, and Ag/AgCl (saturated KCl) as the reference electrode. For the fabrication of the photoanode, as-prepared samples were obtained by mixing a certain amount of ethanol and Nafion solution and 40 mg of as-prepared powder homogeneously. The as-prepared samples were spread on a 15 mm × 20 mm indium−tin oxide (ITO) conducting glass and allowed to dry under ambient conditions. A 300 W Xe arc lamp (PLS-SXE300C/300CUV, Beijing Trusttech Co., Ltd.) with a 420 nm cutoff filter was used as the light source. The electrolyte was a 0.5 mol $L^{-1}$ $Na_2SO_4$ aqueous solution with or without 0.1 mol $L^{-1}$ $K_2S_2O_8$.

Typical electrochemical impedance spectroscopy (EIS) was carried out in the three-electrode system and recorded over a frequency range of 10 mHz−100 kHz with an amplitude of 0.005 V.

**2.5. Computational Parameters.** Periodic density functional theory (DFT) computations were performed using a plane-wave method implemented in the Cambridge Sequential Total Energy Package (CASTEP) code.[39] The local density approximation (LDA)[40] and ultrasoft pseudopotential[41] were used to describe the exchange-correlation effects and electron−ion interactions, respectively. A 340 eV cutoff for the plane-wave basis set was adopted in all computations. The self-consistent convergence accuracy was set at $2 \times 10^{-5}$ eV $atom^{-1}$, the convergence criterion for the force between atoms was 0.05 eV $Å^{-1}$, and the maximum displacement was 0.002 Å. The optimized lattice parameters for BiOCl were found to be $a = b$ = 3.76 Å and $c$ = 7.22 Å and for BiOI were found to be $a = b$ = 3.87 Å and $c$ = 8.96 Å, in good agreement with experimental values ($a = b$ = 3.89 Å and $c$ = 7.35 Å for BiOCl;[42] $a = b$ = 3.99 Å and $c$ = 9.15 Å for BiOI[43]).

For the $BiOI_{(001)}/BiOCl_{(001)}$ interface model, a 3 × 3 10-atomic-layer stoichiometric BiOCl(001) surface slab containing 108 atoms with five bottom layers fixed at the bulk position was used to match a 3 × 3 10-atomic-layer stoichiometric BiOI(001) surface slab containing 108 atoms with five top layers fixed at the bulk position in a supercell. For the $BiOI_{(001)}/BiOCl_{(010)}$ interface model, a 2 × 3 4-atomic-layer stoichiometric BiOCl(010) surface slab containing 72 atoms with 2 bottom layers fixed at the bulk position was used to match a 4 × 3 10-atomic-layer stoichiometric BiOI(001) surface slab containing 144 atoms with 5 top layers fixed at the bulk position. A 15 Å vacuum region was used to prevent interaction between the top and bottom atoms in the periodic slab images. A Morkhorst−Pack mesh[44] of $k$ points, Γ, 2 × 2 × 1 and 1 × 2 × 1 points, was used to sample the two-dimensional Brillouin zone for geometry optimization and to calculate the electronic properties of the $BiOI_{(001)}/BiOCl_{(001)}$ and $BiOI_{(001)}/BiOCl_{(010)}$ interfaces.

## 3. RESULTS AND DISCUSSION

**3.1. Structures of $BiOI_{(001)}/BiOCl_{(001)}$ and $BiOI_{(001)}/BiOCl_{(010)}$ Heterojunctions.** Figure 2 shows X-ray diffraction (XRD) patterns of as-prepared BiOCl-001, BiOCl-010, BiOI, $BiOI_{(001)}/BiOCl_{(001)}$, and $BiOI_{(001)}/BiOCl_{(010)}$ samples. All of the diffraction peaks in the BiOCl-001 and BiOCl-010 nanosheets (Figure 2a,e, respectively) could be indexed to the tetragonal phase of BiOCl (JCPDS No. 06-0249). Similarly, the as-prepared BiOI nanosheets (Figure 2c) could be assigned to the tetragonal phase of BiOI (JCPDS No. 10-0445). A comparison of the XRD patterns of the BiOCl-001 and BiOCl-010 nanosheets (Figure 2a,e) showed that the intensity ratio of the (002) and (200) peaks in BiOCl-001 differs from that in BiOCl-010, reflecting the difference between the surfaces of these two samples, in agreement with the results obtained in the literature.[38] XRD peaks of both tetragonal BiOCl and BiOI could be clearly observed in the $BiOI_{(001)}/BiOCl_{(001)}$ and $BiOI_{(001)}/BiOCl_{(010)}$ heterojunctions (Figure 2b,d, respectively), and no impurity peaks were observed, indicating that the as-prepared heterojunctions were comprised only of BiOCl and BiOI.

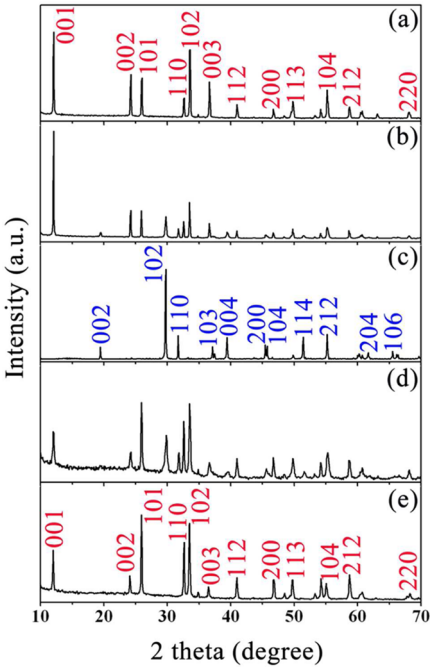


**Figure 2.** XRD patterns for the as-prepared samples: (a) BiOCl-001 nanosheets; (b) $BiOI_{(001)}/BiOCl_{(001)}$ heterojunctions; (c) BiOI nanosheets; (d) $BiOI_{(001)}/BiOCl_{(010)}$ heterojunctions; (e) BiOCl-010 nanosheets.

A scanning electron microscopy (SEM) image (Figure 3$a_1$) showed that the as-prepared BiOCl-001 consisted of large-scale sheet-shaped structures with widths of 1−4 μm. The transmission electron microscopy (TEM) image of an individual BiOCl-001 nanosheet (Figure 3$a_2$) further demonstrated the sheet-shaped architecture of this substrate. The corresponding selected-area electron diffraction (SAED) pattern (Figure 3$a_3$) indicated that the BiOCl-001 nanosheet was a uniform single


DOI: 10.1021/cs501631n
ACS Catal. 2015, 5, 3540−3551

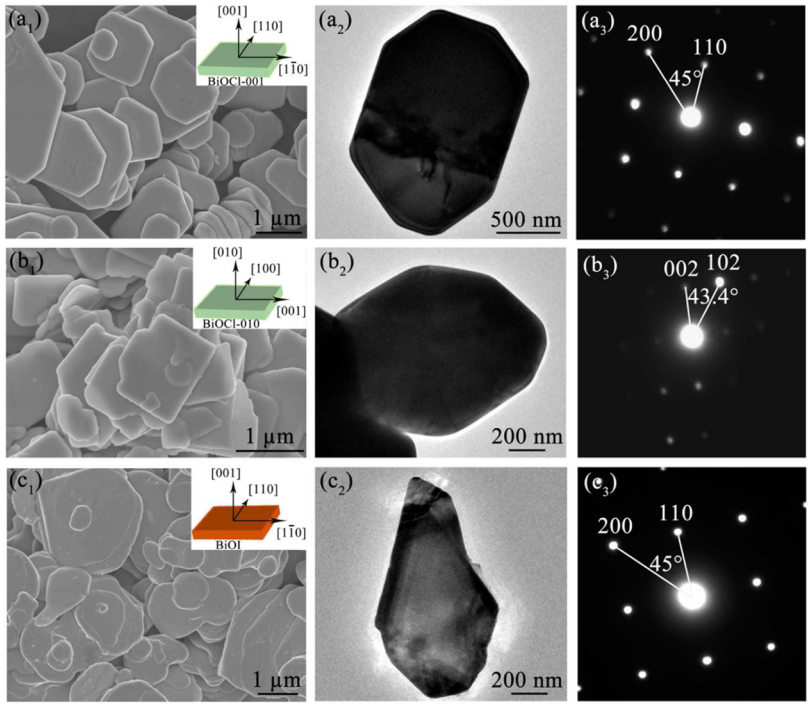


**Figure 3.** SEM images ($a_1$, $b_1$, $c_1$), TEM images ($a_2$, $b_2$, $c_2$), and SAED patterns ($a_3$, $b_3$, $c_3$) of the BiOCl-001 nanosheets ($a_1$−$a_3$), BiOCl-010 nanosheets ($b_1$−$b_3$) and BiOI nanosheets ($c_1$−$c_3$), respectively. Insets give schematic illustrations of the crystal orientation of the as-prepared BiOCl-001 nanosheets, BiOCl-010 nanosheets, and BiOI nanosheets.

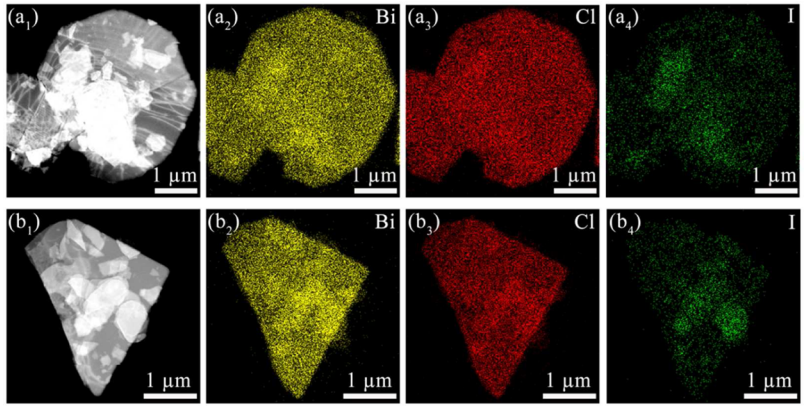


**Figure 4.** STEM-EDS element mapping images of the as-prepared $BiOI_{(001)}/BiOCl_{(001)}$ ($a_1$−$a_4$) and $BiOI_{(001)}/BiOCl_{(010)}$ ($b_1$−$b_4$) heterojunctions.

crystal. The set of diffraction spots could be indexed as the [001] zone axis of tetragonal BiOCl, and the angle between the (200) and (110) planes was 45°, which is identical with the theoretical value. From the symmetry of tetragonal BiOCl, the bottom and top surfaces of the BiOCl-001 nanosheets were identified as {001} facets. From the SEM and TEM images of the BiOCl-010 sample (Figure 3$b_1$,$b_2$, respectively), it can be seen that the BiOCl-010 sample also had well-defined sheet-shaped structures, the width of which was 1−3 $\mu$m. The corresponding SAED pattern (Figure 3$b_3$), indexed as the [010] zone, displayed (002) and (102) planes with an interfacial angle of 43.4°, in agreement with the theoretical value. Hence, the bottom and top surfaces of the BiOCl-010 nanosheets were identified as {010} facets. The SEM and TEM images of the BiOI sample (Figure 3$c_1$,$c_2$, respectively) revealed that the as-prepared BiOI contained irregular nanosheets with widths of ∼1 $\mu$m. The corresponding SAED pattern (Figure 3$c_3$) indicated that the BiOI nanosheets were also enclosed by dominant {001} facets, similar to the BiOCl-001 nanosheets. The structures of the BiOCl-001, BiOCl-010, and BiOI nanosheets are schematically illustrated in the insets of Figure 3.

The SEM images of the $BiOI_{(001)}/BiOCl_{(001)}$ and $BiOI_{(001)}/BiOCl_{(010)}$ heterojunctions are shown in Figure S1 in the Supporting Information. The $BiOI_{(001)}/BiOCl_{(001)}$ and $BiOI_{(001)}/BiOCl_{(010)}$ samples both exhibited BiOCl substrates covered with some thin pieces of BiOI nanosheets, resulting in the rough appearance of the nanosheet surfaces. As shown in Figure 4, scanning transmission electron microscopy−energy dispersive spectrometry (STEM-EDS) elemental mapping was applied to obtain the elemental distributions of Cl and I in the $BiOI_{(001)}/BiOCl_{(001)}$ and $BiOI_{(001)}/BiOCl_{(010)}$ heterojunctions. The red regions in the images (Figure 4$a_3$,$b_3$) correspond to the Cl-containing areas of these heterojunctions, whereas the green regions (Figure 4$a_4$,$b_4$) show the I-containing areas, demonstrating that the core substrate of these two heterojunctions is



DOI: 10.1021/cs501631n
*ACS Catal.* 2015, 5, 3540−3551

BiOCl, whereas the covering sheets are BiOI. This result confirms that BiOI covers the surfaces of the BiOCl nanosheets in both the $BiOI_{(001)}/BiOCl_{(001)}$ and $BiOI_{(001)}/BiOCl_{(010)}$ heterojunctions.

Further detailed structural information about the $BiOI_{(001)}/BiOCl_{(001)}$ and $BiOI_{(001)}/BiOCl_{(010)}$ heterojunctions was obtained using TEM and high-resolution TEM (HRTEM). Figure 5$a_1$,$b_1$ shows typical TEM images of the representative

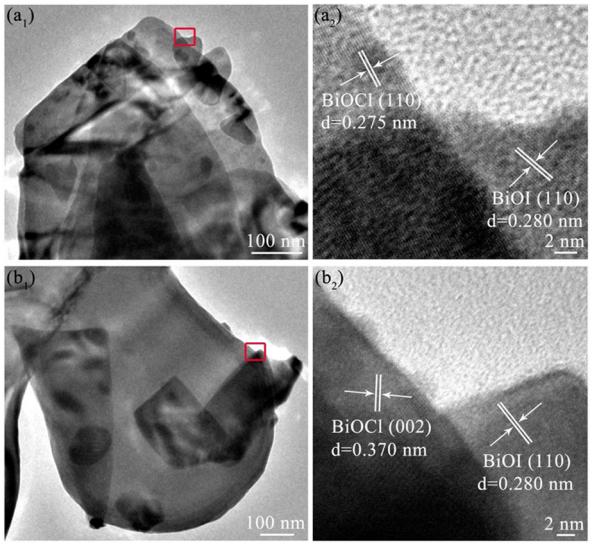


**Figure 5.** TEM ($a_1$, $b_1$) and HRTEM images ($a_2$, $b_2$) of the as-prepared $BiOI_{(001)}/BiOCl_{(001)}$ ($a_1$, $a_2$) and $BiOI_{(001)}/BiOCl_{(010)}$ heterojunctions ($b_1$, $b_2$).

$BiOI_{(001)}/BiOCl_{(001)}$ and $BiOI_{(001)}/BiOCl_{(010)}$ heterojunctions, respectively, with BiOCl substrates covered with thin pieces of BiOI nanosheets, consistent with the observations from SEM experiments. The interactions between BiOCl and BiOI are so strong that ultrasonication during the sample preparation procedure for TEM analysis did not separate them. The HRTEM images of the interfaces of the $BiOI_{(001)}/BiOCl_{(001)}$ and $BiOI_{(001)}/BiOCl_{(010)}$ heterojunctions (Figure 5$a_2$,$b_2$, respectively) are shown in the red square regions indicated in Figure 5$a_1$,$b_1$ and reveal the highly crystalline natures of these heterojunctions. The lattice fringes of 0.275 and 0.280 nm in $BiOI_{(001)}/BiOCl_{(001)}$ (Figure 5$a_2$) corresponded to the (110) plane of BiOCl and the (110) plane of BiOI, respectively. The lattice fringes of 0.370 and 0.280 nm in $BiOI_{(001)}/BiOCl_{(010)}$ (Figure 5$b_2$) were assigned to the (002) plane of BiOCl and the (110) plane of BiOI, respectively. These results and the crystal orientations of the BiOCl-001, BiOCl-010, and BiOI nanosheets indicated that the interfaces of the $BiOI_{(001)}/BiOCl_{(001)}$ heterojunctions were composed of BiOCl(001) and BiOI(001) surfaces, whereas the interfaces of the $BiOI_{(001)}/BiOCl_{(010)}$ heterojunctions were composed of BiOCl(010) and BiOI(001) surfaces.

**3.2. Photocatalytic Activities of $BiOI_{(001)}/BiOCl_{(001)}$ and $BiOI_{(001)}/BiOCl_{(010)}$ Heterojunctions.** The photocatalytic activities of the as-prepared samples were evaluated using the degradation of methyl orange (MO) under visible-light irradiation ($\lambda$ >420 nm). No photolysis of MO was observed after 3 h of visible-light irradiation in the absence of photocatalyst (Figure 6a), demonstrating that MO is chemically stable and difficult to decompose. As the large-band-gap BiOCl (~3.40 eV, as shown in Figure S4 in the Supporting

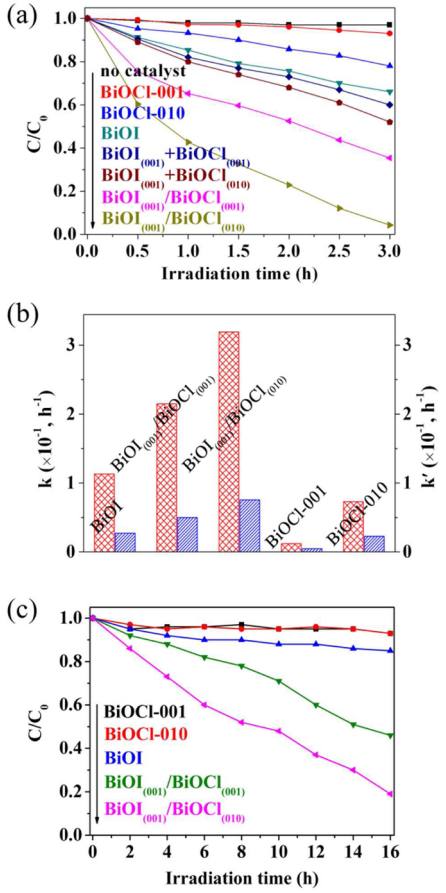


**Figure 6.** (a) Profiles of photocatalytic degradation of MO over the BiOI, BiOCl-001, BiOCl-010 nanosheets, $BiOI_{(001)}/BiOCl_{(001)}$ and $BiOI_{(001)}/BiOCl_{(010)}$ heterojunctions, and mechanically mixed $BiOI_{(001)}$ + $BiOCl_{(001)}$ and $BiOI_{(001)}$ + $BiOCl_{(010)}$ samples under visible-light irradiation ($\lambda$ >420 nm). (b) Degradation rate constants ($k$) and degradation rate constants normalized by surface area ($k'$) for the photocatalytic degradation of MO over the BiOI, BiOCl-001, and BiOCl-010 nanosheets and $BiOI_{(001)}/BiOCl_{(001)}$ and $BiOI_{(001)}/BiOCl_{(010)}$ heterojunctions under visible-light irradiation ($\lambda$ >420 nm). (c) Profiles of photocatalytic degradation of phenol over the BiOI, BiOCl-001, BiOCl-010 nanosheets and $BiOI_{(001)}/BiOCl_{(001)}$ and $BiOI_{(001)}/BiOCl_{(010)}$ heterojunctions under visible-light irradiation ($\lambda$ >420 nm).

Information) cannot be excited by visible-light irradiation, the removal of MO using BiOCl-001 was as low as 4%. However, BiOCl-010 showed a relatively better photocatalytic performance, with a degradation ratio of 22%, via an indirect dye photosensitization process.[38] Though BiOI has strong absorption in the visible-light range, only 34% of MO was photodegraded in the presence of BiOI after visible-light irradiation for 3 h. The as-prepared 3/7 (I/Cl molar ratio) $BiOI_{(001)}/BiOCl_{(001)}$ and 3/7 $BiOI_{(001)}/BiOCl_{(010)}$ heterojunctions exhibited higher photocatalytic activity than pure BiOCl-001, pure BiOCl-010, and pure BiOI under visible-light irradiation. Interestingly, 3/7 $BiOI_{(001)}/BiOCl_{(010)}$ degraded MO by 95% in 3 h, which was superior to 3/7 $BiOI_{(001)}/BiOCl_{(001)}$, which degraded MO by 65% in 3 h. To evaluate the significance of the heterojunction interaction for the photocatalytic activity of $BiOI_{(001)}/BiOCl_{(001)}$ and $BiOI_{(001)}/BiOCl_{(010)}$, photocatalytic degradation experiments using mechanically mixed $BiOI_{(001)}$ + $BiOCl_{(001)}$ and $BiOI_{(001)}$ + $BiOCl_{(010)}$ (3/7 I/Cl molar ratio) were also carried out (Figure


DOI: 10.1021/cs501631n
ACS Catal. 2015, 5, 3540−3551

6a). The mechanically mixed samples showed much lower photocatalytic activities than $BiOI_{(001)}/BiOCl_{(001)}$ and $BiOI_{(001)}/BiOCl_{(010)}$. This result implies that the interaction between BiOCl and BiOI plays an important role in the improved photocatalytic activity of the BiOI/BiOCl heterojunctions.

In heterojunction materials, the proportion of the components has an important effect on the photocatalytic performance. Figure S2 in the Supporting Information shows the rate constants ($k$) for the photocatalytic degradation of MO using visible-light irradiation obtained for $BiOI_{(001)}/BiOCl_{(001)}$ and $BiOI_{(001)}/BiOCl_{(010)}$ heterojunctions with different I/Cl molar ratios. All of the BiOI/BiOCl heterojunctions exhibited higher visible-light photodegradation activities for photodegradation of MO than the three individual materials. In addition, the visible-light photocatalytic performances of $BiOI_{(001)}/BiOCl_{(010)}$ were superior to those of the $BiOI_{(001)}/BiOCl_{(001)}$ heterojunctions at all molar ratios. It can be deduced that the superior photocatalytic activity of $BiOI_{(001)}/BiOCl_{(010)}$ is not significantly affected by the proportion of its components.

The visible-light photodegradation of MO may take place via an indirect dye photosensitization process, as seen with BiOCl-010, which is strongly dependent on the surface area. The BET surfaces of BiOCl-001, BiOCl-010, BiOI, $BiOI_{(001)}/BiOCl_{(001)}$, and $BiOI_{(001)}/BiOCl_{(010)}$ have been given in Table S1 in the Supporting Information. The degradation rate constant $k$ and the degradation rate constant normalized by the surface area $k'$ are compared in Figure 6b. The normalized $k'$ value of $BiOI_{(001)}/BiOCl_{(010)}$ was still higher than that of $BiOI_{(001)}/BiOCl_{(001)}$, indicating that the higher photocatalytic activity of $BiOI_{(001)}/BiOCl_{(010)}$ is related to the heterojunction structure rather than differences in the surface area.

In order to verify that the higher visible-light photocatalytic activity of $BiOI_{(001)}/BiOCl_{(010)}$ can be mainly attributed to its unique heterojunction structure and is not induced by the dye photosensitization process, we have chosen phenol, which has no indirect dye photosensitization process, as the target pollutant. The activity for phenol photodegradation over BiOCl-001, BiOCl-010, BiOI, $BiOI_{(001)}/BiOCl_{(001)}$, and $BiOI_{(001)}/BiOCl_{(010)}$ is shown in Figure 6c. Both BiOCl-001 and BiOCl-010 almost have no visible-light photocatalytic activity for phenol degradation, indicating that phenol has no dye photosensitization process over these two nanosheets. The $BiOI_{(001)}/BiOCl_{(001)}$ and $BiOI_{(001)}/BiOCl_{(010)}$ heterojunctions exhibit higher photocatalytic activity over phenol in comparison to that of BiOCl-001, BiOCl-010, and BiOI under visible-light irradiation. Significantly, the phenol photogradation over $BiOI_{(001)}/BiOCl_{(010)}$ is greater than that over $BiOI_{(001)}/BiOCl_{(010)}$, and this demonstrates that the photocatalytic activity of $BiOI_{(001)}/BiOCl_{(010)}$ is indeed enhanced in comparison with that of $BiOI_{(001)}/BiOCl_{(001)}$.

The stability of a photocatalyst is important for its assessment and application. The stability of 3/7 $BiOI_{(001)}/BiOCl_{(010)}$ during photocatalytic reactions was explored using recycling tests, and the results of these tests are shown in Figure S3 in the Supporting Information. No obvious catalyst deactivation was found, indicating that the as-prepared $BiOI_{(001)}/BiOCl_{(010)}$ heterojunctions were very stable during photocatalysis. In addition, the XRD patterns of 3/7 $BiOI_{(001)}/BiOCl_{(010)}$ before and after the degradation are shown in Figure S5 in the Supporting Information. In comparison with $BiOI_{(001)}/BiOCl_{(010)}$ before the degradation, the XRD peaks of $BiOI_{(001)}/BiOCl_{(010)}$ after the degradation were well maintained, indicating that the structure of $BiOI_{(001)}/BiOCl_{(010)}$ did not change during the MO degradation.

### 3.3. Mechanisms Accounting for the Enhanced Visible-Light Photocatalytic Activity of $BiOI_{(001)}/BiOCl_{(001)}$ and $BiOI_{(001)}/BiOCl_{(010)}$.

On the basis of the above HRTEM results for the $BiOI_{(001)}/BiOCl_{(001)}$ and $BiOI_{(001)}/BiOCl_{(010)}$ interfaces, two theoretical models of the interfaces, consisting of BiOCl(001) or BiOCl(010) surfaces interfacing with BiOI(001) surfaces were built to investigate the interaction mechanisms between BiOCl and BiOI. A 3 × 3 BiOCl(001) surface slab (Figure 7A(a)) and a 3 × 3 BiOI(001) surface slab (Figure 7A(b)) were matched to build the $BiOI_{(001)}/BiOCl_{(001)}$ interface model (Figure 7A(c)). As shown in Figure 7A(d), the lattice mismatch between the 3 × 3 BiOCl(001) and 3 × 3 BiOI(001) surface slabs along the $a$ direction is $(3a_{BiOI(001)} - 3a_{BiOCl(001)})/3a_{BiOCl(001)} = 2.93\%$, and

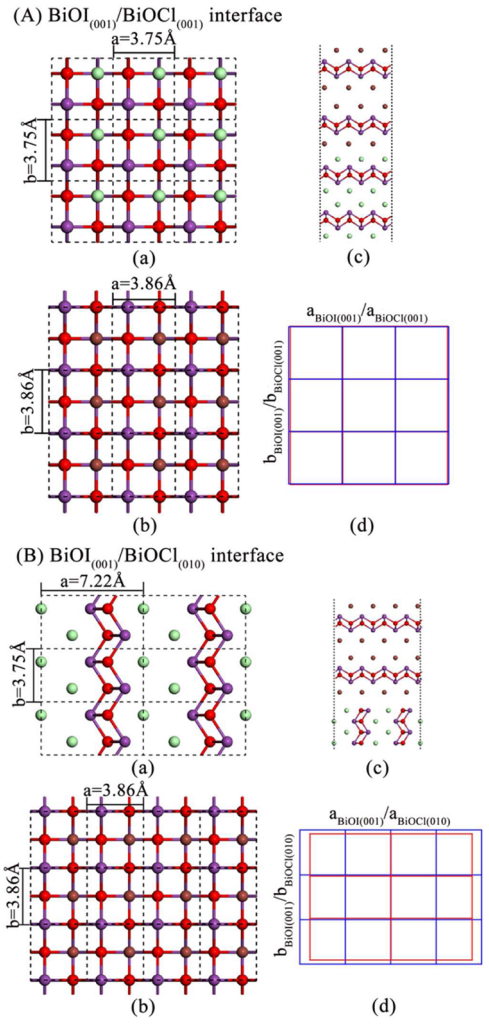


**Figure 7.** Models for simulating the interfaces between BiOCl and BiOI. (A) $BiOI_{(001)}/BiOCl_{(001)}$ interface: (a) BiOCl(001)-(3× 3) surface; (b) BiOI(001)-(3 × 3)surface; (c) side view of the $BiOI_{(001)}/BiOCl_{(001)}$ interface before geometry optimization; (d) schematic of the interfacial lattice mismatch. The blue and red lines represent the BiOCl and BiOI lattices, respectively. (B) $BiOI_{(001)}/BiOCl_{(010)}$ interface: (a) BiOCl(010)-(2 × 3) surface; (b) BiOI(001)-(4 × 3) surface; (c) side view of the $BiOI_{(001)}/BiOCl_{(010)}$ interface before geometry optimization; (d) schematic of the interfacial lattice mismatch.



DOI: 10.1021/cs501631n
ACS Catal. 2015, 5, 3540−3551

the mismatch along the $b$ direction is $(3b_{BiOI(001)} - 3b_{BiOCl(001)})/3b_{BiOCl(001)} = 2.93\%$. For the $BiOI_{(001)}/BiOCl_{(010)}$ interface model (Figure 7B(c)), a 2 × 3 BiOCl(010) surface slab (Figure 7B(a)) was used to match a 4 × 3 BiOI(001) surface slab (Figure 7B(b)). As shown in Figure 7B(d), the lattice mismatch between 2 × 3 BiOCl(010) and 4 × 3 BiOI(001) surface slabs along the $a$ direction is $(4a_{BiOI(001)} - 2a_{BiOCl(010)})/2a_{BiOCl(010)} = 6.93\%$, whereas that along the $b$ direction is $(3b_{BiOI(001)} - 3b_{BiOCl(010)})/3b_{BiOCl(010)} = 2.93\%$. $BiOI_{(001)}/BiOCl_{(001)}$ has a better lattice match, but $BiOI_{(001)}/BiOCl_{(010)}$ has the superior visible-light photocatalytic activity. In order to understand this phenomenon, we further studied the interface interaction of these two heterojunctions.

The interface adhesion energies ($E_{ad}$) of the $BiOI_{(001)}/BiOCl_{(001)}$ and $BiOI_{(001)}/BiOCl_{(010)}$ interfaces were used to judge the stabilities of these systems and were obtained according to

$$E_{ad001\text{-}001} = E_{com} - E_{BiOI(001)} - E_{BiOCl(001)} \quad (1)$$

$$E_{ad001\text{-}010} = E_{com} - E_{BiOI(001)} - E_{BiOCl(010)} \quad (2)$$

where $E_{com}$, $E_{BiOCl(001)}$, $E_{BiOCl(010)}$, and $E_{BiOI(001)}$ represent the total energies of the relaxed BiOI/BiOCl interfaces, BiOCl(001), BiOCl(010), and BiOI(001) surfaces, respectively. If the obtained $E_{ad}$ value is negative, the interface is stable, and lower values correspond to more stable interfaces. The $E_{ad}$ values for $BiOI_{(001)}/BiOCl_{(001)}$ and $BiOI_{(001)}/BiOCl_{(010)}$ interfaces were calculated to be −0.39 and −0.68 eV, respectively, indicating that these two interfaces were stable. Though the $BiOI_{(001)}/BiOCl_{(001)}$ interface has a better lattice match, the $BiOI_{(001)}/BiOCl_{(010)}$ interface is more stable. Thus, it can be concluded that the interaction mechanisms of these two interfaces are different.

The interaction mechanisms of the $BiOI_{(001)}/BiOCl_{(001)}$ and $BiOI_{(001)}/BiOCl_{(010)}$ interfaces were further investigated by Mulliken charge population analyses (Table 1) combined with X-ray photoelectron spectroscopy (XPS) (Figure 8). The structures of the $BiOI_{(001)}/BiOCl_{(001)}$ and $BiOI_{(001)}/BiOCl_{(010)}$ interfaces following geometry optimization are shown in Figure 8A(a),B(a), respectively. Admittedly, the absolute magnitudes of the atomic charge yielded by the population analysis have little physical meaning, but there is some useful information in the relative values of the Mulliken population. In the $BiOI_{(001)}/BiOCl_{(001)}$ interface, because the atomic radius of Cl (0.99 Å) is smaller than that of I (1.33 Å), the interaction between the X (X = Cl, I) anions and the $[Bi_2O_2]^{2+}$ layer at the interface becomes stronger, resulting in the X anions capturing more electrons from $[Bi_2O_2]^{2+}$. Thus, the calculated charges on the Bi cations increased to 1.41e and 1.23e from 1.38e for the pure BiOCl(001) surface and 1.19e for the pure BiOI (001) surface, respectively. The effective displacement of valence electron density away from the Bi atomic nucleus results in a reduction of electrical screening of the inner shells and a blue shift of the Bi 4f peak in $BiOI_{(001)}/BiOCl_{(001)}$ in comparison with the same peak in BiOCl-001 and BiOI (Figure 8A(b)). The calculated charge on the Cl anion (−0.47e) of the $BiOI_{(001)}/BiOCl_{(001)}$ interface was less than that of the BiOCl(001) surface (−0.51e), while the I anion showed a charge increase to −0.35e in comparison to the I anion of the BiOI(001) surface (−0.31e), ascribed to the electronegativity of I being higher than that of Cl. The electrical screening of the Cl inner shells decreased owing to the decrease in valence electron charge, resulting in a blue shift of the Cl 2p peak of the $BiOI_{(001)}/BiOCl_{(001)}$ heterojunction in comparison with that of pure BiOCl-001 (Figure 8A(d)). The increase of electrical screening of the I inner shells resulted in the red shift of the I 3d peak of $BiOI_{(001)}/BiOCl_{(001)}$ in comparison with pure BiOI (Figure 8A(e)). The calculated charges on the O anions (−0.91e and −0.90e) of the $BiOI_{(001)}/BiOCl_{(001)}$ interface were the same as those of pure BiOCl (001) (−0.91e) and pure BiOI (001) (−0.90e). The O anions are located at the sublayer interface and are not directly involved in the interfacial interaction; consequently, the O 1s peak of $BiOI_{(001)}/BiOCl_{(001)}$ remained at the same binding energy as observed for BiOCl-001 and BiOI (Figure 8A(c)). Similar to the case for $BiOI_{(001)}/BiOCl_{(001)}$, the Bi 4f peak (Figure 8B(b)) and Cl 2p peak of $BiOI_{(001)}/BiOCl_{(010)}$ (Figure 8B(d)) moved to higher binding energy regions in comparison with the individual materials. A comparison of Figure 8A(d),B(d) shows that the Cl 2p peak of BiOCl-001 is different from that of BiOCl-010, confirming the different surface structures of these two individual materials. Since the surface O anions of BiOCl(010) directly interacts with the $I^-$ layer of the BiOI(001) surface, the charges on the O anions in the $BiOI_{(001)}/BiOCl_{(010)}$ interface decreased to −0.91e and −0.89e from −0.93e in BiOCl(001) and −0.90e in BiOI(001), respectively, and the charge on the I anion at the interface decreased to −0.25e in comparison with that of the BiOI(001) surface (−0.31e). The decreased charges on the O and I anions correspond to the blue shifts observed in the O 2p and I 3d peaks of the $BiOI_{(001)}/BiOCl_{(010)}$ heterojunction in comparison with the two individual materials (Figure 8B(c),B-(c),B(e)). On the basis of the Mulliken charge population and XPS analyses, the existence of an interaction between BiOCl and BiOI in both the $BiOI_{(001)}/BiOCl_{(001)}$ and $BiOI_{(001)}/BiOCl_{(010)}$ heterojunctions and a difference in the interaction mechanisms for the $BiOI_{(001)}/BiOCl_{(001)}$ and $BiOI_{(001)}/BiOCl_{(010)}$ interfaces can be confirmed.

Photocurrents were measured for BiOCl-001, BiOCl-010, BiOI, $BiOI_{(001)}/BiOCl_{(001)}$, and $BiOI_{(001)}/BiOCl_{(010)}$ to investigate the photogenerated charge transfer efficiencies. As shown in Figure 9a, all of the samples were prompt in generating photocurrent with a reproducible response to on/off visible-light irradiation cycles, demonstrating effective charge transfer and successful electron collection for the samples within the photoelectrochemical cell (PEC). Under visible-light irradiation, pure BiOCl-001 and pure BiOCl-010 showed almost no photocurrent responses, owing to the wide band gap of BiOCl. The photocurrent responses of $BiOI_{(001)}/BiOCl_{(001)}$ and $BiOI_{(001)}/BiOCl_{(010)}$ were about 2 and 3 times higher, respectively, than that of the pure BiOI, indicating that the

**Table 1. Mulliken Charge Population on the Bi, O, Cl, and I Atoms for Pure BiOCl(001), BiOCl(010), and BiOI(001) Surfaces and $BiOI_{(001)}/BiOCl_{(001)}$ and $BiOI_{(001)}/BiOCl_{(010)}$ Heterojunctions**

| | charge population | | | |
|---|---|---|---|---|
| species | Bi | O | Cl | I |
| BiOCl(001) surface | 1.38 | −0.91 | −0.51 | |
| BiOCl(010) surface | 1.39 | −0.93 | −0.49 | |
| BiOI(001) surface | 1.19 | −0.90 | | −0.31 |
| $BiOI_{(001)}/BiOCl_{(001)}$ interface | 1.41/1.23 | −0.91/−0.90 | −0.47 | −0.35 |
| $BiOI_{(001)}/BiOCl_{(010)}$ interface | 1.35/1.16 | −0.91/−0.89 | −0.47 | −0.25 |



DOI: 10.1021/cs501631n
ACS Catal. 2015, 5, 3540−3551

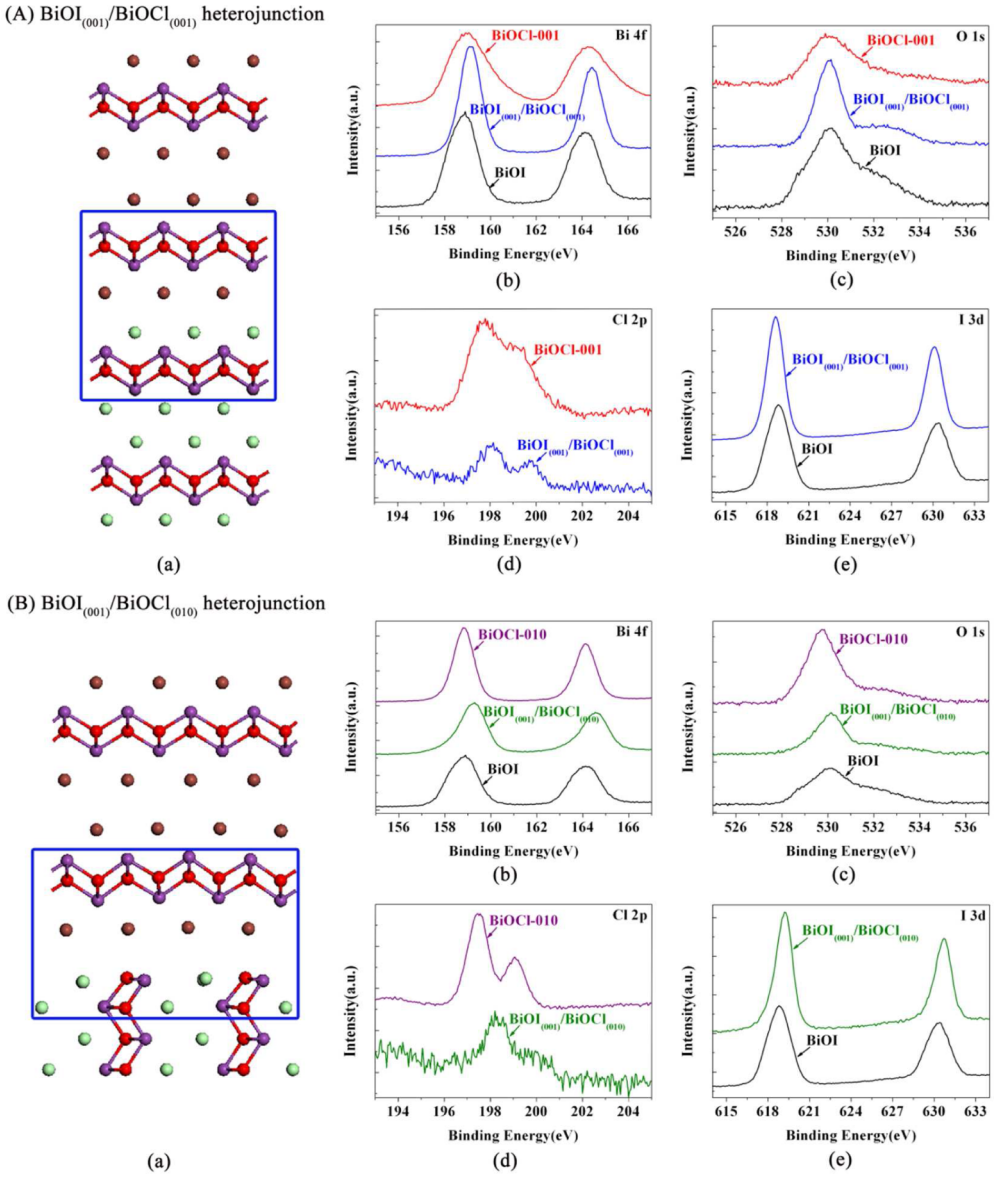


**Figure 8.** XPS spectra for as-prepared samples. (A) $BiOI_{(001)}/BiOCl_{(001)}$ heterojunction: (a) the model of $BiOI_{(001)}/BiOCl_{(001)}$ interface after geometry optimization; (b) Bi 4f of BiOCl-001, $BiOI_{(001)}/BiOCl_{(001)}$, and BiOI; (c) O 1s of BiOCl-001, $BiOI_{(001)}/BiOCl_{(001)}$, and BiOI; (d) Cl 2p of BiOCl-001 and $BiOI_{(001)}/BiOCl_{(001)}$; (e) I 3d of $BiOI_{(001)}/BiOCl_{(001)}$ and BiOI. (B) $BiOI_{(001)}/BiOCl_{(010)}$ heterojunction: (a) the model of $BiOI_{(001)}/BiOCl_{(010)}$ interface after geometry optimization; (b) Bi 4f of BiOCl-010, $BiOI_{(001)}/BiOCl_{(010)}$, and BiOI; (c) O 1s of BiOCl-010, $BiOI_{(001)}/BiOCl_{(010)}$, and BiOI; (d) Cl 2p of BiOCl-010 and $BiOI_{(001)}/BiOCl_{(010)}$; (e) I 3d of $BiOI_{(001)}/BiOCl_{(010)}$ and BiOI.

photogenerated electrons and holes in BiOI are able to separate and subsequently transfer to BiOCl because of the synergetic effect between the BiOI and BiOCl semiconductors. In comparison with $BiOI_{(001)}/BiOCl_{(001)}$, $BiOI_{(001)}/BiOCl_{(010)}$ exhibited an increased photocurrent density, demonstrating an enhanced photogenerated charge transfer efficiency of the $BiOI_{(001)}/BiOCl_{(010)}$ heterojunction.

In general, the photocatalytic activity of a heterojunction ($\eta_{PC}$) has a positive correlation with light harvesting ($\eta_{LH}$), charge separation ($\eta_{CS}$), and charge injection ($\eta_{CI}$). The $\eta_{CS}$ and $\eta_{CI}$ values were estimated using[23−26]

$$\eta_{PC} = \eta_{LH} \times \eta_{CS} \times \eta_{CI} \quad (3)$$

where $\eta_{PC}$ and $\eta_{LH}$ are the photocurrent density and the photon absorption rate, respectively. The $\eta_{CS}$ value indicates the fraction of photogenerated charges that reach the interface and achieve separation of electrons and holes; this process is closely related to the band match between the two individual materials. The $\eta_{CI}$ value indicates the fraction of separated electrons that reach the surfaces of receiving material and subsequently transfer to the adsorbates during consecutive surface reactions; this process does not have much dependence on the band match. In order to investigate the $\eta_{CS}$ and $\eta_{CI}$ values of the $BiOI_{(001)}/BiOCl_{(001)}$ and $BiOI_{(001)}/BiOCl_{(010)}$ heterojunctions, the photocurrents of these two heterojunctions in $Na_2SO_4$ solutions with $K_2S_2O_8$ were measured under visible-light irradiation (Figure 9b). $K_2S_2O_8$ was used as an electron scavenger to consume the separated electrons that reached the BiOCl surfaces. In the presence of $K_2S_2O_8$, the value of $\eta_{CI}$ becomes 1, because the electrons that reach the surface are completely consumed. Thus, the photocurrent of sample in an aqueous solution with $K_2S_2O_8$ becomes


DOI: 10.1021/cs501631n
ACS Catal. 2015, 5, 3540−3551

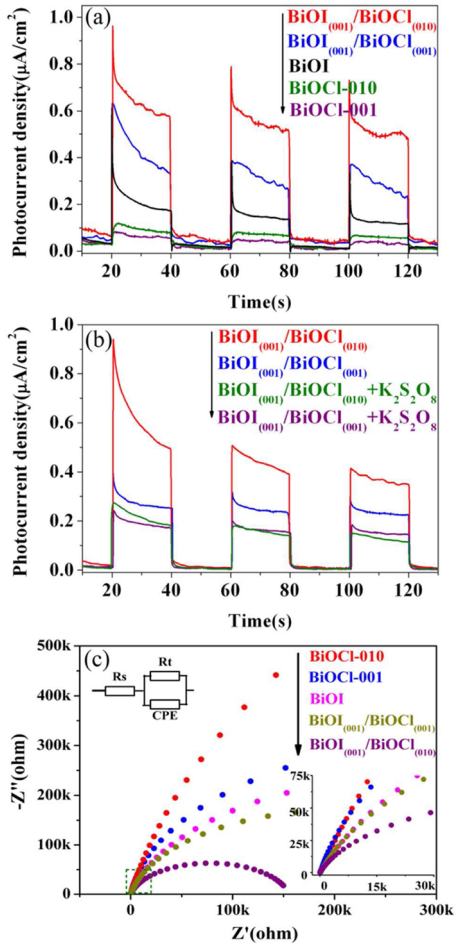


**Figure 9.** (a) Photocurrent responses of the pure BiOCl-001, BiOCl-010, BiOI, $BiOI_{(001)}/BiOCl_{(001)}$, and $BiOI_{(001)}/BiOCl_{(010)}$ in 0.5 M $Na_2SO_4$ aqueous solutions under visible-light irradiation. (b) Photocurrent response of $BiOI_{(001)}/BiOCl_{(001)}$ and $BiOI_{(001)}/BiOCl_{(010)}$ heterojunctions in 0.5 M $Na_2SO_4$ aqueous solutions with 0.1 M $K_2S_2O_8$ under visible-light irradiation. (c) EIS Nyquist plots of pure BiOCl-001, BiOCl-010, BiOI, $BiOI_{(001)}/BiOCl_{(001)}$, and $BiOI_{(001)}/BiOCl_{(010)}$ under visible-light irradiation. The left inset represents a simulated circuit diagram. The high-resolution EIS in the high-frequency zone is shown in the right inset.

$$I_{PC}^{KSO} = \eta_{LH} \times \eta_{CS} \quad (4)$$

As shown in Figure S4a in the Supporting Information, the $BiOI_{(001)}/BiOCl_{(001)}$ and $BiOI_{(001)}/BiOCl_{(010)}$ heterojunctions have similar band gap energies and photon absorption intensities in the visible-light region. It can be assumed that the estimated $\eta_{LH}$ values are not very different for the $BiOI_{(001)}/BiOCl_{(001)}$ and $BiOI_{(001)}/BiOCl_{(010)}$ samples and $\eta_{LH}$ can be treated as a constant in this study. According to eq 4, the photocurrent responses measured in $Na_2SO_4$ solution with $K_2S_2O_8$ are positively correlated with $\eta_{CS}$. Figure 9b shows that the photocurrent responses of the $BiOI_{(001)}/BiOCl_{(001)}$ and $BiOI_{(001)}/BiOCl_{(010)}$ heterojunctions in $Na_2SO_4$ solution with $K_2S_2O_8$ are almost the same, indicating that these two heterojunctions have the same $\eta_{CS}$ values. This result can be attributed to the similar band match of the $BiOI_{(001)}/BiOCl_{(001)}$ and $BiOI_{(001)}/BiOCl_{(010)}$ heterojunctions (Figure S4). Thus, the higher $\eta_{CI}$ value is the main cause of the higher photocurrent response and better visible-light photocatalytic activity of $BiOI_{(001)}/BiOCl_{(010)}$.

In addition, the typical electrochemical impedance spectroscopy (EIS) of BiOCl-001, BiOCl-010, BiOI, $BiOI_{(001)}/BiOCl_{(001)}$, and $BiOI_{(001)}/BiOCl_{(010)}$ was measured and is shown in Figure 9c, in order to investigate the charge transfer process more deeply. The semicircle in the Nyquist plot can be simulated well by an electrical equivalent-circuit model (Figure 9c, left inset).[45,46] For the model shown, the charge-transfer resistance $R_t$ is in parallel with the double-layer capacitance (CPE), and this combination is in serial with the total ohmic resistance of the electrolyte solution resistance $R_s$.[47] The fitting results were calculated on the basis of this model (Table S2 in the Supporting Information).The semicircle radius of EIS plots can be used to evaluate the efficiency of charge separation and transfer. A smaller semicircle radius corresponds to a lower charge-transfer resistance value of $R_t$ and reflects higher electron−hole separation and transfer efficiencies and vice versa.[48−50] As shown by Figure 9c, $BiOI_{(001)}/BiOCl_{(001)}$ and $BiOI_{(001)}/BiOCl_{(010)}$ both have a smaller semicircle radius of EIS plots and lower $R_t$ values in comparison to those of pure BiOCl-001, BiOCl-010, and BiOI. The $BiOI_{(001)}/BiOCl_{(010)}$ features an even smaller semicircle radius with an lower $R_t$ value, in contrast to that of $BiOI_{(001)}/BiOCl_{(001)}$, which indicates its more efficient interfacial charge-carrier separation and transfer. As the high-resolution EIS in the high-frequency zone shows (Figure 9c, right inset), the slope of the EIS plot sequence of as-prepared samples is BiOCl-010 > BiOCl-001 > BiOI > $BiOI_{(001)}/BiOCl_{(001)}$ > $BiOI_{(001)}/BiOCl_{(010)}$. $BiOI_{(001)}/BiOCl_{(010)}$ has the smallest slope of the EIS plot, which confirms again that the transfer processes of photogenerated charge carriers are indeed improved by its unique heterojunction structure.

We have calculated the electron difference density maps and Mulliken charge population analyses for the $BiOI_{(001)}/BiOCl_{(001)}$ and $BiOI_{(001)}/BiOCl_{(010)}$ interfaces. By combination of the electron difference density maps (Figure 10$a_1$,$a_2$) and Mulliken charge population analyses (Figure 10$b_1$,$b_2$), it can be seen that the [X] (X = Cl, I) layers carry negative charges and the $[Bi_2O_2]$ layers carry positive charges in both the $BiOI_{(001)}/BiOCl_{(001)}$ and $BiOI_{(001)}/BiOCl_{(010)}$ interfaces. This charge separation results in a self-induced internal electric field along the *c* axis in the $BiOI_{(001)}/BiOCl_{(001)}$ interface, as shown in Figure 10$c_1$. In contrast, in the $BiOI_{(001)}/BiOCl_{(010)}$ interface, the self-induced internal electric field of the BiOI slab is along the *c* axis and the self-induced internal electric field of BiOCl slab is along the *b* axis, as is illustrated in Figure 10$c_2$.

The proposed photodegradation mechanisms for MO using the $BiOI_{(001)}/BiOCl_{(001)}$ and $BiOI_{(001)}/BiOCl_{(010)}$ heterojunctions are shown in Figure 11. BiOI acts as a visible-light sensitizer and generates the electrons and holes in both heterojunctions. Under the band-match conditions of the BiOI/BiOCl heterojunctions, the photogenerated electrons in BiOI transfer into the BiOCl; meanwhile, the photogenerated holes in BiOI are effectively collected at the surfaces of BiOI, owing to the self-induced internal electric field of BiOI. In this way, the photogenerated electron−hole pairs are effectively separated. This process is the same in both heterojunctions; thus, the $\eta_{CS}$ value of $BiOI_{(001)}/BiOCl_{(001)}$ is equal to that of $BiOI_{(001)}/BiOCl_{(010)}$. However, once the photogenerated electrons reach BiOCl, the electron transfer pathway in $BiOI_{(001)}/BiOCl_{(001)}$ is different from that in $BiOI_{(001)}/BiOCl_{(010)}$. As schematically illustrated in Figure 11a, the self-induced internal electric fields of BiOCl are perpendicular to the $BiOI_{(001)}/BiOCl_{(001)}$ heterojunction. Therefore, the photo-


DOI: 10.1021/cs501631n
ACS Catal. 2015, 5, 3540−3551

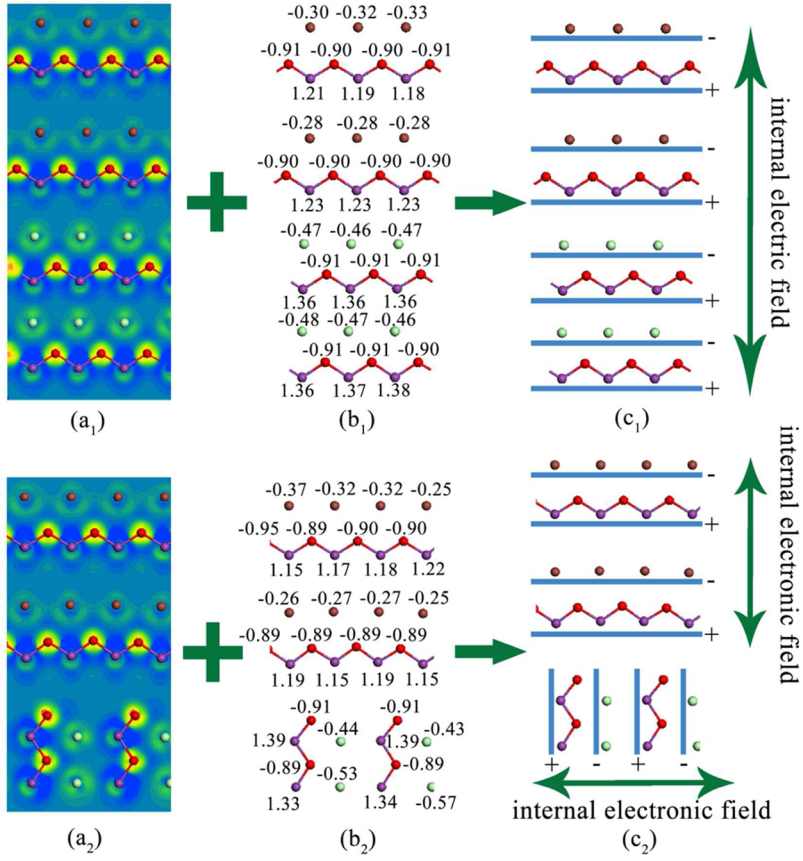


**Figure 10.** For the $BiOI_{(001)}/BiOI_{(001)}$ interface: ($a_1$) electron difference density map; ($b_1$) Mulliken charge population on Bi, O, Cl, and I atoms; ($c_1$) orientation of self-induced internal electric field. For the $BiOI_{(001)}/BiOCl_{(010)}$ interface: ($a_2$) electron difference density map; ($b_2$) Mulliken charge population on Bi, O, Cl, and I atoms; ($c_2$) orientation of self-induced internal electric field.

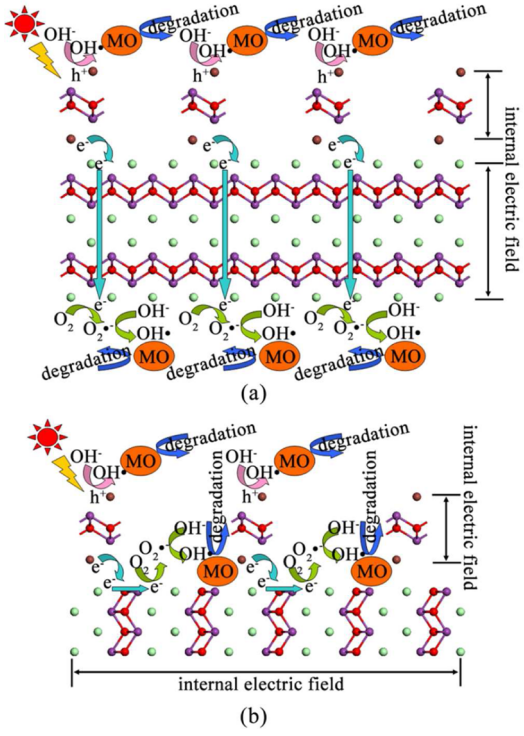


**Figure 11.** Proposed photodegradation mechanism of MO over $BiOI_{(001)}/BiOCl_{(001)}$ (a) and $BiOI_{(001)}/BiOCl_{(010)}$ heterojunctions (b), respectively.

generated electrons transfer along the *c* axis direction assisted by the internal electric fields and reach the bottom surface of the BiOCl component to inject into the adsorbates during subsequent surface reactions. In this process, some of the photogenerated electrons are lost because of the long diffusion distance, resulting in the low $\eta_{CI}$ value of the $BiOI_{(001)}/BiOCl_{(001)}$ heterojunction. In contrast, in $BiOI_{(001)}/BiOCl_{(010)}$, the self-induced internal electric fields of BiOCl are parallel to the heterojunction, as illustrated in Figure 11b. The self-induced internal electric fields of BiOCl along the *b* axis direction result in the photogenerated electrons rapidly reaching the top surfaces of BiOCl, and then these photogenerated electrons inject into adsorbates during surface reactions. The short diffusion distance of photogenerated electrons in this process decreases the loss of photogenerated electrons, leading to the higher $\eta_{CI}$ value of $BiOI_{(001)}/BiOCl_{(010)}$.

## 4. CONCLUSION

In summary, we have designed and synthesized $BiOI_{(001)}/BiOCl_{(001)}$ and $BiOI_{(001)}/BiOCl_{(010)}$ photocatalysts by combining heterojunction nanostructure construction with a crystal facet engineering method. HRTEM analyses confirmed the presences of $BiOI_{(001)}/BiOCl_{(001)}$ and $BiOI_{(001)}/BiOCl_{(010)}$ interfaces in the $BiOI_{(001)}/BiOCl_{(001)}$ and $BiOI_{(001)}/BiOCl_{(010)}$ heterojunctions, respectively. By combining DFT calculations with XPS analysis, we found that although the lattice mismatch of the $BiOI_{(001)}/BiOCl_{(010)}$ interface is larger than that of the $BiOI_{(001)}/BiOCl_{(001)}$ interface, $BiOI_{(001)}/BiOCl_{(010)}$ is more


DOI: 10.1021/cs501631n
ACS Catal. 2015, 5, 3540−3551

stable, which could be attributed to the different interaction mechanisms of these two interfaces. As the formation of heterojunctions can significantly reduce the recombination and accelerate the separation rate of photogenerated charge carriers, both of the heterojunctions were more photocatalytically more active than their individual components. Moreover, the visible-light photocatalytic activity of $BiOI_{(001)}/BiOCl_{(010)}$ was superior to that of $BiOI_{(001)}/BiOCl_{(001)}$. $BiOI_{(001)}/BiOCl_{(001)}$ had the same $\eta_{CS}$ value as $BiOI_{(001)}/BiOCl_{(010)}$ because of their similar band-match situations. Because the self-induced internal electric fields of BiOCl slabs in the $BiOI_{(001)}/BiOCl_{(001)}$ and $BiOI_{(001)}/BiOCl_{(010)}$ heterojunctions were perpendicular and parallel to the two heterojunctions, respectively, the $\eta_{CI}$ value of $BiOI_{(001)}/BiOCl_{(010)}$ was higher than that of $BiOI_{(001)}/BiOCl_{(001)}$ owing to an optimized electron transfer pathway. This difference in electron transfer pathways was the main factor accounting for the higher visible-light photocatalytic activity of the $BiOI_{(001)}/BiOCl_{(010)}$ heterojunction. The results obtained in our study offer a promising direction for the design of more practical and efficient visible-light photocatalysts.

## ■ ASSOCIATED CONTENT

### Supporting Information

The Supporting Information is available free of charge on the ACS Publications website at DOI: 10.1021/cs501631n.

Additional characterization data, including SEM images of $BiOI_{(001)}/BiOCl_{(001)}$ and $BiOI_{(001)}/BiOCl_{(010)}$ heterojunctions (Figure S1), the degradation rate constants for photocatalytic degradation of MO over the BiOI, BiOCl-001, and BiOCl-010 nanosheets and $BiOI_{(001)}/BiOCl_{(001)}$ and $BiOI_{(001)}/BiOCl_{(010)}$ heterojunctions with different I/Cl molar ratios under visible-light ($\lambda$ >420 nm) irradiation (Figure S2), recycling test for the photocatalytic degradation of MO on $BiOI_{(001)}/BiOCl_{(010)}$ heterojunctions under visible-light ($\lambda$ >420 nm) irradiation (Figure S3), UV−vis spectra of BiOI, BiOCl-001, BiOCl-010, $BiOI_{(001)}/BiOCl_{(001)}$, and $BiOI_{(001)}/BiOCl_{(010)}$ and VB XPS spectra of BiOI, BiOCl-001, and BiOCl-010 (Figure S4), XRD patterns for the $BiOI_{(001)}/BiOCl_{(010)}$ heterojunction before and after degradation (Figure S5), BET surface areas of BiOI, $BiOI_{(001)}/BiOCl_{(001)}$, $BiOI_{(001)}/BiOCl_{(010)}$, BiOCl-001, and BiOCl-010 (Table S1), and parameters of equivalent circuits for the impedance data of BiOCl-001, BiOCl-010, BiOI, $BiOI_{(001)}/BiOCl_{(001)}$, and $BiOI_{(001)}/BiOCl_{(010)}$ (Table S2) (PDF)

## ■ AUTHOR INFORMATION


### Corresponding Author

*W.F.: tel, 86-531-88366330; fax, 86-531-88365174; e-mail, fwl@sdu.edu.cn.

### Author Contributions

⊥These authors contributed equally to this study and share the first authorship.


### Notes

The authors declare no competing financial interest.

## ■ ACKNOWLEDGMENTS

This work was supported by the National Natural Science Foundation of China (Grant No. 21173131), 973 Program of China (Grant Nos. 2009CB930103 and 2010CB933504), Independent Innovation Foundation of Shandong University (Grant No. 2012TS212), and Taishan Scholar Project of Shandong Province.

## ■ REFERENCES


(1) Fujishima, A.; Honda, K. *Nature* **1972**, *238*, 37−38.
(2) Hoffmann, M. R.; Martin, S. T.; Choi, W. Y.; Bahnemann, D. W. *Chem. Rev.* **1995**, *95*, 69−96.
(3) Zou, Z. G.; Ye, J. H.; Sayama, K.; Arakawa, H. *Nature* **2001**, *414*, 625−627.
(4) Asahi, R.; Morikawa, T.; Ohwaki, T.; Aoki, K.; Taga, Y. *Science* **2001**, *293*, 269−271.
(5) Maeda, K.; Teramura, K.; Lu, D. L.; Takata, T.; Saito, N.; Inoue, Y.; Domen, K. *Nature* **2006**, *440*, 295−295.
(6) Varghese, O. K.; Paulose, M.; LaTempa, T. J.; Grimes, C. A. *Nano Lett.* **2009**, *9*, 731−737.
(7) Yi, Z. G.; Ye, J. H.; Kikugawa, N.; Kako, T.; Ouyang, S. X.; Stuart-Williams, H.; Yang, H.; Cao, J. Y.; Luo, W. J.; Li, Z. S.; Liu, Y.; Withers, R. L. *Nat. Mater.* **2010**, *9*, 559−564.
(8) Lü, X. J.; Huang, F. Q.; Mou, X. L.; Wang, Y. M.; Xu, F. F. *Adv. Mater.* **2010**, *22*, 3719−3722.
(9) Wang, Q.; Zhang, M. A.; Chen, C. C.; Ma, W. H.; Zhao, J. C. *Angew. Chem., Int. Ed.* **2010**, *49*, 7976−7979.
(10) Zhang, J.; Xu, Q.; Feng, Z.; Li, M.; Li, C. *Angew. Chem., Int. Ed.* **2008**, *47*, 1766−1769.
(11) Kudo, A.; Miseki, Y. *Chem. Soc. Rev.* **2009**, *38*, 253−278.
(12) Hou, Y.; Zuo, F.; Dagg, A.; Feng, P. Y. *Nano Lett.* **2012**, *12*, 6464−6473.
(13) Kim, E. S.; Nishimura, N.; Magesh, G.; Kim, J. Y.; Jang, J. W.; Jun, H.; Kubota, J.; Domen, K.; Lee, J. S. *J. Am. Chem. Soc.* **2013**, *135*, 5375−5383.
(14) Yan, S. C.; Lv, S. B.; Li, Z. S.; Zou, Z. G. *Dalton Trans.* **2010**, *39*, 1488−1491.
(15) Liu, X. J.; Pan, L. K.; Lv, T.; Lu, T.; Zhu, G.; Sun, Z.; Sun, C. Q. *Catal. Sci. Technol.* **2011**, *1*, 1189−1193.
(16) Hong, S. J.; Lee, S.; Jang, J. S.; Lee, J. S. *Energy Environ. Sci.* **2011**, *4*, 1781−1787.
(17) Ge, L.; Han, C. C.; Liu, J. *Appl. Catal., B* **2011**, *108−109*, 100−107.
(18) Wang, Y. J.; Shi, R.; Lin, J.; Zhu, Y. F. *Energy Environ. Sci.* **2011**, *4*, 2922−2929.
(19) Pan, C. S.; Xu, J.; Wang, Y. J.; Li, D.; Zhu, Y. F. *Adv. Funct. Mater.* **2012**, *22*, 1518−1524.
(20) An, X. Q.; Yu, J. C.; Wang, Y.; Hu, Y. M.; Yu, X. L.; Zhang, G. J. *J. Mater. Chem.* **2012**, *22*, 8525−8531.
(21) Yang, M. Q.; Weng, B.; Xu, Y. J. *Langmuir* **2013**, *29*, 10549−10558.
(22) Zhou, W. J.; Yin, Z. Y.; Du, Y. P.; Huang, X.; Zeng, Z. Y.; Fan, Z. X.; Liu, H.; Wang, J. Y.; Zhang, H. *Small* **2013**, *9*, 140−147.
(23) Zhang, H. J.; Liu, L.; Zhou, Z. *RSC Adv.* **2012**, *2*, 9224−9229.
(24) Dotan, H.; Sivula, K.; Graetzel, M.; Rothschild, A.; Warren, S. C. *Energy Environ. Sci.* **2011**, *4*, 958−964.
(25) Abdi, F. F.; Firet, N.; Van de Krol, R. *ChemCatChem* **2013**, *5*, 490−496.
(26) Jeong, H. W.; Jeon, T. H.; Jang, J. S.; Choi, W.; Park, H. *J. Phys. Chem. C* **2013**, *117*, 9104−9112.
(27) Zhang, N.; Yang, M. Q.; Tang, Z. R.; Xu, Y. J. *ACS Nano* **2014**, *8*, 623−633.
(28) Zhang, X.; Ai, Z. H.; Jia, F. L.; Zhang, L. Z. *J. Phys. Chem. C* **2008**, *112*, 747−753.
(29) Chang, X. F.; Huang, J.; Cheng, C.; Sui, Q.; Sha, W.; Ji, G. B.; Deng, S. B.; Yu, G. *Catal. Commun.* **2010**, *11*, 460−464.
(30) Zhang, W. D.; Zhang, Q.; Dong, F. *Ind. Eng. Chem. Res.* **2013**, *52*, 6740−6746.
(31) Xiong, J. Y.; Cheng, G.; Li, G. F.; Qin, F.; Chen, R. *RSC Adv.* **2011**, *1*, 1542−1553.
(32) Ye, L. Q.; Zan, L.; Tian, L. H.; Peng, T. Y.; Zhang, J. J. *Chem. Commun.* **2011**, *47*, 6951−6953.




DOI: 10.1021/cs501631n
*ACS Catal.* 2015, 5, 3540−3551

(33) Guan, M. L.; Xiao, C.; Zhang, J.; Fan, S. J.; An, R.; Cheng, Q. M.; Xie, J. F.; Zhou, M.; Ye, B. J.; Xie, Y. *J. Am. Chem. Soc.* **2013**, *135*, 10411−10417.
(34) Fang, Y. F.; Huang, Y. P.; Yang, J.; Wang, P.; Cheng, G. W. *Environ. Sci. Technol.* **2011**, *45*, 1593−1600.
(35) Zhang, J.; Shi, F. J.; Lin, J.; Chen, D. F.; Gao, J. M.; Huang, Z. X.; Ding, X. X.; Tang, C. C. *Chem. Mater.* **2008**, *20*, 2937−2941.
(36) Ai, Z. H.; Ho, W.; Lee, S.; Zhang, L. Z. *Environ. Sci. Technol.* **2009**, *43*, 4143−4150.
(37) Li, Y. Y.; Wang, J. S.; Yao, H. C.; Dang, L. Y.; Li, Z. J. *J. Mol. Catal. A: Chem.* **2011**, *334*, 116−122.
(38) Jiang, J.; Zhao, K.; Xiao, X. Y.; Zhang, L. Z. *J. Am. Chem. Soc.* **2012**, *134*, 4473−4476.
(39) Clark, S. J.; Segall, M. D.; Pickard, C. J.; Hasnip, P. J.; Probert, M. J.; Refson, K.; Payne, M. C. *Z. Kristallogr.* **2005**, *220*, 567−570.
(40) Ceperley, D. M.; Alder, B. J. *Phys. Rev. Lett.* **1980**, *45*, 566−569.
(41) Rappe, A. M.; Rabe, K. M.; Kaxiras, E.; Joannopoulos, J. D. *Phys. Rev. B: Condens. Matter Mater. Phys.* **1990**, *41*, 1227−1230.
(42) Keramidas, K. G.; Voutsas, G. P.; Rentzeperis, P. I. *Z. Kristallogr.* **1993**, *205*, 35−40.
(43) Keller, E.; Kraemer, V. *Z. Naturforsch., B* **2005**, *60*, 1255−1263.
(44) Monkhorst, H. J.; Pack, J. *Phys. Rev. B: Solid State* **1976**, *13*, 5188−5192.
(45) Ma, T. Y.; Dai, S.; Jaroniec, M.; Qiao, S. Z. *Angew. Chem., Int. Ed.* **2014**, *53*, 7281−7285.
(46) Li, Q.; Meng, H.; Yu, J. G.; Xiao, W.; Zheng, Y. Q.; Wang, J. *Chem. - Eur. J.* **2014**, *20*, 1176−1185.
(47) Jo, W. J.; Jang, J.; Kong, K.; Kang, H. J.; Kim, J. Y.; Jun, H.; Parmar, K. P. S.; Lee, J. S. *Angew. Chem., Int. Ed.* **2012**, *51*, 3147−3151.
(48) Bai, X. J.; Wang, L.; Zong, R. L.; Zhu, Y. F. *J. Phys. Chem. C* **2013**, *117*, 9952−9961.
(49) Zhu, Y. Y.; Liu, Y. F.; Lv, Y. H.; Ling, Q.; Liu, D.; Zhu, Y. F. *J. Mater. Chem. A* **2014**, *2*, 13041−13048.
(50) Wang, L.; Shang, J.; Hao, W. C.; Jiang, S. Q.; Huang, S. H.; Wang, T. M.; Sun, Z. Q.; Du, Y.; Dou, S. X.; Xie, T. F.; Wang, D. J.; Wang, J. O. *Sci. Rep.* **2014**, *7*, 7384.



DOI: 10.1021/cs501631n
*ACS Catal.* 2015, 5, 3540−3551